PAPER

Check for updates

Fabrication of a P–Si/ZnO heterojunction based on galvanic cell driven and the complete degradation of RhB *via* fast charge transfer†

Xiaoyu Yang,[a] Lin Wu,[a,b] Baoguo Zhang,[a] Jingwang Li,[a] Yifan Shen,[a] Ying Liu*[a] and Ya Hu ID *[a,b]

Semiconductor heterojunctions can significantly enhance photocatalytic degradation efficiency by facilitating rapid interfacial charge transfer. This article is based on the galvanic-cell driven principle; porous silicon (P–Si) was prepared by the carbon-catalytic etching method, and ZnO was loaded on its surface *via* electroless chemical deposition technology to form a P–Si/ZnO heterojunction, which was applied to the degradation of Rhodamine B (RhB). At a deposition temperature of 90 °C, a flawless 1D hexagonal prism structure of ZnO was formed, allowing the P–Si/ZnO heterojunction to completely degrade RhB within 2 hours with a degradation rate of 100%. Compared with a single P–Si material, the degradation performance is improved by 1.7 times. The formation of the built-in electric field and the rapid charge transfer at the heterojunction interface realized the complete degradation of RhB organic pollutants. After 20 cycles of use, the photocatalytic degradation rate remains above 70%, demonstrating excellent stability and recyclability.

[a]*Key Laboratory of Hubei Province for Coal Conversion and New Carbon Materials, School of Chemistry and Chemical Engineering, Wuhan University of Science and Technology, Wuhan 430081, China. E-mail: huya@wust.edu.cn, liuying-9325@wust.edu.cn*
[b]*Academy of Green Manufacturing Engineering, Wuhan University of science and technology, Wuhan 430081, China*
†Electronic supplementary information (ESI) available. See DOI: https://doi.org/10.1039/d3nr04078j

Ya Hu is currently an associate professor at the school of chemistry and chemical engineering, Wuhan University of Science and Technology (WUST), China. She received her Ph.D. degree in Condensed Matter Physics from Beijing Normal University in 2015. She engaged in the research work in Professor Stuart Parkin's group in Max Planck Institute of Microstructure Physics, Germany served as post-doctor research fellow and then joined in WUST. From 2018 she works as a visiting researcher at division of solid-state electronics, Uppsala University, Sweden. Her research interests include electrochemical etching technology and application of ultrafine nano silicon materials.

Ya Hu

1. Introduction

Azo dyes represented by Rhodamine B (RhB) are one of the most extensively applied dyes in the dye industry and have certain risks to human health and the environment. Currently, the common methods for degrading RhB in the industry include advanced ozone oxidation, anaerobic treatment, biofilm technology, the Fenton method, and photocatalytic degradation.[1–6] Among these methods, the photocatalytic degradation of RhB has gradually become a research hotspot due to its advantages in energy conservation and cost-effectiveness. Semiconductor materials have stable properties and wide bandgaps, and can absorb light in a wide spectral range, so they are widely used in photocatalytic degradation technology.[7] However, in photocatalytic degradation technology, using a single semiconductor material encounters issues of poor stability and inefficient utilization of photogenerated carriers, leading to photo corrosion and low catalytic degradation efficiency.[8–12] Therefore, it is customary to construct semiconductor heterojunctions with controllable structures for application in photocatalytic degradation technology. For instance, Li *et al.*[13] prepared g-C_3N_4/TiO_2 composite materials by the seed-induced solvothermal method for the degradation of methyl orange under visible-light irradiation. The results showed that the g-C_3N_4/TiO_2 composites exhibited superior photocatalytic activity under visible light irradiation, and the degradation rate is significantly higher than that of the single

components of g-C$_3$N$_4$ and TiO$_2$. On the other hand, Hamza et al.[14] synthesized PbCrO$_4$/ZnO nanocomposites, which can effectively reduce the recombination of photogenerated carriers and enhance the photocatalytic degradation performance of RhB. Wang and Thi Hoa et al.[15,16] prepared Si/ZnO heterojunctions using the hydrothermal method and observed that the built-in electric field generated by the space charge region of the heterojunction can greatly reduce the recombination rate of photogenerated carriers. But the Si substrate is an untreated single crystal Si, so the Si/ZnO heterojunction cannot effectively utilize sunlight and can only function within a specific spectral range, resulting in limited degradation efficiency.

Porous silicon (P–Si) exhibits superior physicochemical properties compared with bulk materials. It can effectively absorb photons in the visible light region (accounting for more than 45% of solar energy), and has a porous structure that can efficiently capture photons and quickly conduct them to the reactant surface. Therefore, P–Si has been widely applied in the field of photocatalytic degradation.[17] Nevertheless, it also faces challenges, such as difficulty utilizing solar UV energy and severe photo corrosion. ZnO is a wide-band gap semiconductor material with a band gap of 3.2 eV, and the exciton binding energy is as high as 60 meV. It has exceptional photoresponse capability and excellent photostability, effectively mitigating photo corrosion.[18–21] The combined use of P–Si and ZnO can promote the separation of electron–hole pairs at the interface, reduce recombination, increase the contact area with reactants, and improve light absorption capability and reaction rate. Rangelova et al.[22] prepared a SiO$_2$/ZnO composite material by the sol–gel method for photocatalytic degradation of malachite green. The degradation rate reached 90% after 40 minutes of UV irradiation when the ZnO content was 10%. In another work, Wen et al.[23] utilized first-principles calculations to investigate the electronic structure, magnetism properties, and photocatalytic properties of the Si-doped g-ZnO monolayer. They observed that Si doping was beneficial for exciting electrons, reducing the bandgap between the Fermi level and conduction band, and enhancing the absorption capacity of visible light. Lan et al.[24] used a metal-induced wet-etching technique to grow a ZnO/Si nanowire array on a P-type silicon wafer for catalytic degradation of methylene blue under light irradiation. The results showed that after loading ZnO onto the Si surface, the sample's light absorption rate increased to over 94%, and the photodegradation efficiency increased from 48.9% to 62.0%. Consequently, the construction of a P–Si/ZnO heterojunction can enhance the photoelectric conversion performance of the material and accelerate the separation and migration rate of photogenerated carriers, thereby promoting photocatalytic degradation performance.[16,23,25,26] For the preparation methods reported above, it is a huge challenge to have both simple operation and low cost.

This article employs a two-step method to synthesize P–Si/ZnO heterojunction composites based on the galvanic cell-driven mechanism. Firstly, carbon catalytic etching is used to fabricate P–Si, followed by electroless chemical deposition of

ZnO on its surface. Finally, a P–Si/ZnO heterojunction structure is obtained, which achieves the complete degradation of RhB. By adjusting the deposition temperature, P–Si and ZnO form an optimal 1D heterojunction structure. The micromorphology and crystal structure of the materials were characterized by XRD, SEM, and XPS, which proved the successful preparation of the P–Si/ZnO heterojunction. Under the irradiation of UV and visible light, 5 mg L^{-1} RhB solution was used as the simulated pollutant and combined with UV-Vis, the photocatalytic degradation performance and recyclability of the materials were evaluated. Meanwhile, the photocatalytic degradation process and mechanism of RhB by the P–Si/ZnO heterojunction were investigated through quenching experiments and electrochemical characterization.

2. Experimental

2.1 Preparation of materials

Preparation of P–Si. A single crystal silicon wafer with a resistivity ranging from 1 to 10 Ω cm, a size of 2.0 cm × 2.0 cm, and an orientation of p-type (100) was ultrasonically cleaned with deionized water, acetone, and ethanol for 15 minutes, respectively. Subsequently, the silicon wafer was thoroughly rinsed with deionized water and dried. The clean silicon wafer was put into the polytetrafluoroethylene (PTFE) lining, followed by the addition of 0.2 g graphite particles, 4.58 M HF (wt. 40%), and 0.98 M H$_2$O$_2$ (wt. 30%) to form a mixed etchant solution. Then the PTFE lining was placed in a vacuum oven preheated to 30 °C for 5 h. After the reaction, the silicon wafer was taken out and cleaned, and then immersed in diluted HF solution for 20 s to remove residual graphite particles and silicon dioxide on the surface of the silicon wafer. Finally, the silicon wafer was dried for further use.

Preparation of the P–Si/ZnO heterojunction. The P–Si/ZnO heterojunction was prepared by electroless chemical deposition technology by adjusting the oil bath temperature and the loading amount of ZnO during the reaction process. First, pure aluminum sheets of 2 cm × 5 cm were ultrasonically cleaned with deionized water, acetone, and anhydrous ethanol for 10 minutes. Afterward, the sheets were thoroughly rinsed with deionized water and dried for later use. Then a double-ended wire with alligator clips was used, one end was attached to the cleaned aluminum sheet, and the other end was fastened to the porous silicon, and immersed in an electrolyte solution composed of 0.25 mM AgNO$_3$, 25 mM Zn(NO$_3$)$_2$, and 25 mM hexamethylenetetramine (HMT), ensuring that the alligator clips were above the liquid surface. Finally, the samples were heated at oil bath temperatures of 70 °C, 80 °C, 90 °C, 100 °C, and 120 °C for 3 hours to obtain samples at different temperatures, which were marked as P–Si/ZnO-70 °C, P–Si/ZnO-80 °C, P–Si/ZnO-90 °C, P–Si/ZnO-100 °C, and P–Si/ZnO-120 °C.

2.2 Material characterization

The crystal structure of the sample was determined by the X-ray diffraction technique using a SmartLab SE with Cu Kα

radiation. The surface morphology and compositional content of the sample were characterized by combining a field emission scanning electron microscope FEI MOVA 400 Nano and energy-dispersive X-ray spectrometer (EDS). X-ray photoelectron spectroscopy (XPS) was performed using an AXIS SUPRA+ to investigate the chemical state and bond types of the material surface. Ultraviolet–Visible Diffuse Reflectance Spectra (UV-Vis DRS) were recorded by using a UV-2550 UV-Vis spectrophotometer with barium sulfate employed as the reflection standard, and the test wavelength range was from 200 nm to 800 nm.

2.3 Evaluation of photocatalytic activity

Under UV and visible light irradiation, the P–Si/ZnO heterojunction carried out photocatalytic degradation of the RhB solution. In the experiment, a sample with an area of 2 cm × 2 cm was placed in 30 mL of RhB solution with an initial concentration of 5 mg L^{-1} and maintained in darkness for 60 minutes to achieve adsorption–desorption equilibrium. A 300 W xenon lamp (CEL-PE300-4A) was used as a solar light simulator (AM 1.5G, 100 mW cm^{-2}), and placed 20 cm away from the reaction device to reduce thermal effects. At intervals of 30 minutes, a 3 mL sample solution was taken out from the reactor and the absorbance of the RhB solution was measured at the maximum absorption wavelength of 554 nm using a UV-2550 ultraviolet-visible spectrophotometer.

2.4 Electrochemical measurements

The electrochemical experiment was carried out on a CHI760E electrochemical workstation. The workstation adopts a three-electrode system, the P–Si/ZnO heterojunction as the working electrode, a Pt wire as the counter electrode, and Ag/AgCl as the reference electrode. During the experiment, a 5 mg L^{-1} RhB electrolyte solution was used. The entire experimental process was performed in a customized electrochemical cell equipped with an O-shaped quartz window. The back of the working electrode is coated with a liquid gallium/indium alloy mixture to form an ohmic contact. The linear sweep voltammetry curve (LSV) was recorded under two conditions, dark and light, in a bias potential range of −1.5 to 1.5 V. The aforementioned xenon lamp was utilized as a solar simulator. The i–t curve was measured at a bias voltage of 1.5 V (vs. Ag/AgCl). In the light environment, the Electrochemical Impedance Spectroscopy (EIS) test was performed, in the frequency range between 10^5 and 10^{-2} Hz, under open-circuit potential.

3. Results and discussion

3.1 Characterization

Fig. 1 shows the schematic diagram of the preparation process for the P–Si/ZnO heterojunction. The preparation process is based on the galvanic cell driven principle, utilizing the difference in electronegativity between graphite particles and silicon wafers to etch in the HF and H_2O_2 corrosive solution, thereby obtaining P–Si (Fig. 1a and b).

Next, P–Si is cleansed with a diluted HF solution to remove residual graphite particles and impurities on the surface. Finally, ZnO nanowires were deposited on the surface of P–Si by using the electroless chemical deposition technique. In this process, aluminum sheets function as sacrificial anodes that oxidize and generate an electron source, which is utilized to reduce silver ions on the cathodic surface of P–Si to elemental
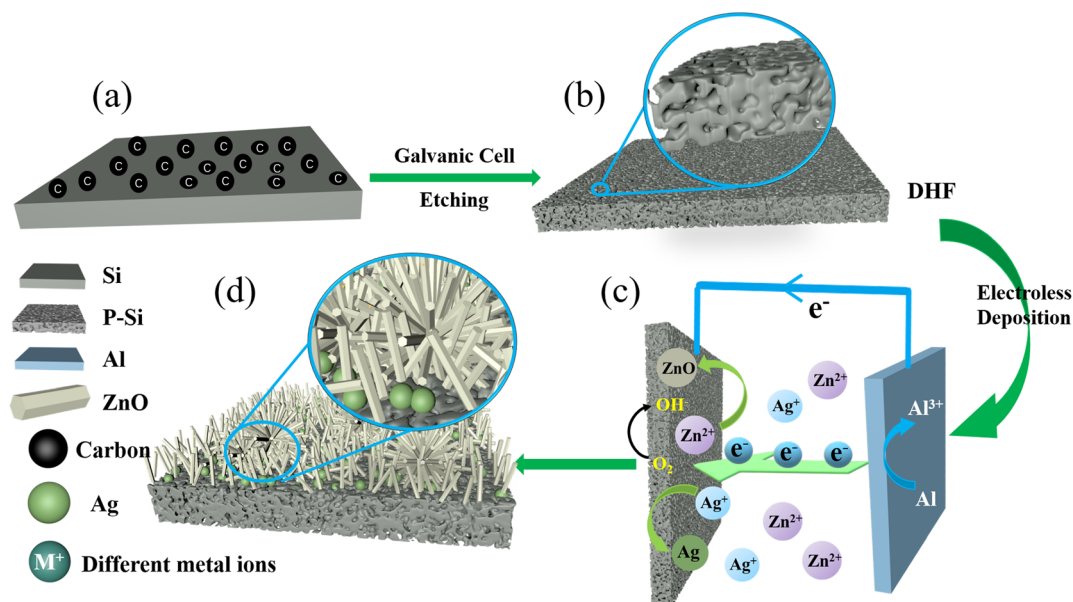

Fig. 1 Synthesis process schematic of the P–Si/ZnO heterojunction. (a) Graphite particles are deposited and distributed on the surface of single-crystal silicon. (b) Three-dimensional structure diagram of P–Si. (c) Mechanism diagram of electroless deposition of ZnO on the porous silicon surface. (d) Three-dimensional structure diagram of the P–Si/ZnO heterojunction.

silver. Simultaneously, HMT hydrolyzes OH^- and Zn^{2+} to form zinc hydroxide, which dehydrates at a certain temperature to produce ZnO, and O_2 in the solution obtains e^- to form OH^-, which promotes the generation of ZnO (as shown in Fig. 1c). Finally, the P–Si/ZnO heterojunction shown in Fig. 1d is obtained.

In this paper, the crystallinity of P–Si and the P–Si/ZnO heterojunction was characterized by the X-ray diffraction (XRD) technique. The XRD spectrum of P–Si obtained by graphite particle catalyzed etching is shown in Fig. 2, showing a single diffraction peak at 69.52°, corresponding to the Si (400) crystal plane diffraction peak of single-crystal Si. After loading ZnO onto the P–Si surface, the characteristic diffraction peaks of ZnO match the standard PDF card (JSPD#36-1451) and appear at diffraction angles of 31.75°, 34.39°, 36.23°, 47.25°, 56.32°, 62.80°, 66.13°, 68.04°, and 77.48°, corresponding to the crystal planes (100), (002), (101), (102), (110), (103), (200), (112), and (202), respectively. The asterisks in the figure, from left to right, correspond to the (111), (200), and (220) crystal planes of silver particles, matching the standard PDF card (JSPD#04-0783) for metallic silver and consistent with the reduction of silver ions to elemental silver on the P–Si cathode surface in Fig. 1.

The microstructure of the P–Si and P–Si/ZnO heterojunction is shown in Fig. 3a–f. The figure compares the micromorphology of the P–Si surface after the deposition of ZnO nanowires at different oil bath temperatures (70 °C, 80 °C, 90 °C, 100 °C, and 120 °C). P–Si with a uniform pore size distribution of about 200 nm, prepared by graphite particle catalyzed etching, is shown in Fig. 3a. At a deposition temperature of 70 °C, the lateral growth of ZnO nuclei initiates, forming hexagonal crystal structures (Fig. 3b). At 80 °C, the growth rate of ZnO nuclei increases, leading to the emergence of polycrystalline overlapping (Fig. 3c).[27] When the deposition temperature is raised to 90 °C, as shown in Fig. 3d, the crystal nucleus

growth activity is further accelerated, the single crystal length tends towards homogeneity, and the ZnO hexagonal crystal structure is complete. The inset in the figure depicts the cross-sectional image of the P–Si surface deposited with ZnO under this condition. At 100 °C, the formation of the ZnO tubular structure commences, as illustrated in Fig. 3e. As the reaction temperature increases, the hydrolysis of HMT to NH_3 becomes slower, causing more Zn^{2+} to convert into ZnO crystal nuclei under the influence of OH^- so that more ZnO nuclei with active sites gather spontaneously and form tubular structures in the reaction environment.[28] When the synthesis temperature is raised to 120 °C, as shown in Fig. 3f, compared with 100 °C, more Zn^{2+} and NH_3 were generated in the reaction system, which reduced the formation rate of ZnO crystal nuclei.[28] The slow formation of ZnO crystal nuclei reduces the opportunity for the formation of nanotubes, while partial erosion occurs on the single crystal (0001) face, and the crystals located at the lower end remain intact.[27] The Energy Dispersive X-ray Spectrometer (EDS) image demonstrates the successful preparation of ZnO nanowires and Ag particles.

In Fig. 4a, the XPS spectra reveal that P–Si/ZnO is primarily composed of Zn, O, Ag, Si, and C elements. In the high-resolution XPS spectra of Zn 2p (Fig. 4b), two peaks appearing at 1044.73 eV and 1021.8 eV are attributed to Zn $2p_{1/2}$ and Zn $2p_{3/2}$, respectively, with a spin–orbit spacing of 22.93 eV, indicating that the Zn element mainly exists in the form of Zn^{2+} in the sample.[21,24,29] Fig. 4c shows the XPS spectra of O 1s, with three characteristic peaks at binding energies of 531.21 eV, 530.40 eV, and 529.40 eV, corresponding to C–OH, Zn–O, and Ag–O–Ag, respectively.[30] The characteristic peak positions at 374.2 eV and 368.2 eV in Fig. 4d are attributed to Ag $3d_{3/2}$ and Ag $3d_{5/2}$, respectively.[24] Fig. 5e shows the XPS spectrum of Si 2p, where the two characteristic peaks at 102.64 eV and 99.61 eV binding energies correspond to the inner-shell electrons of Si 2p, respectively, corresponding to Si–O and Si.[17] In the XPS spectra of C 1s (Fig. 4f), the characteristic peak at 284.8 eV is attributed to residual graphite particles in the sample. These results are consistent with XRD and SEM, which further proves the successful preparation of P–Si/ZnO composite materials.

3.2 Photocatalytic properties

To evaluate the photocatalytic degradation performance of the P–Si/ZnO heterojunction for RhB, we conducted UV-Vis absorption spectroscopy, as shown in Fig. 5a–d. Under dark conditions, the sample primarily removed RhB from the solution through adsorption, reaching adsorption–desorption equilibrium within 60 minutes. When exposed to UV and visible light, no obvious change was observed in RhB within 2 hours, indicating that RhB had excellent stability under illumination. The degradation rate of RhB by P–Si can reach 57.95% within 2 hours. After loading ZnO nanowires on its surface, the degradation efficiencies of RhB by P–Si/ZnO-70 °C, P–Si/ZnO-80 °C, P–Si/ZnO-90 °C, P–Si/ZnO-100 °C, and P–Si/ZnO-120 °C within 2 hours are 69.48%, 74.09%, 100%, 76.53%, and 80%, respectively, which is consistent with the SEM results. Furthermore, Fig. 5c and d illustrates the linear
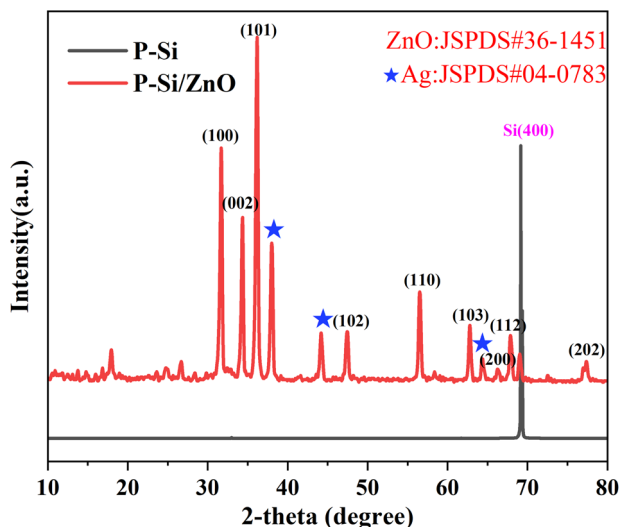

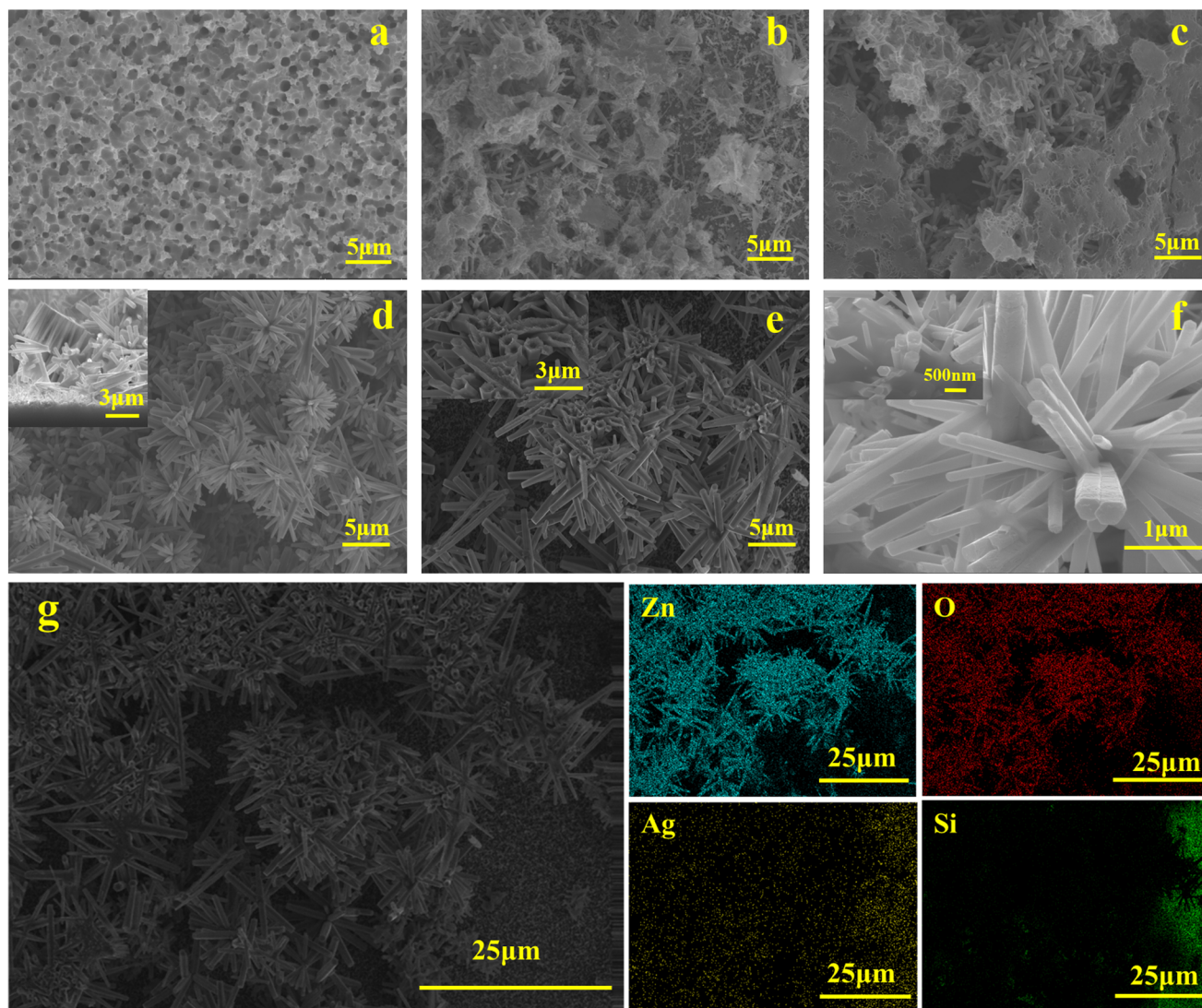**Fig. 2** XRD patterns of P−Si and P−Si/ZnO heterojunction.

Fig. 3 SEM images of (a) P–Si, (b) P–Si/ZnO-70 °C, (c) P–Si/ZnO-80 °C, (d) P–Si/ZnO-90 °C, (e) P–Si/ZnO-100 °C, and (f) P–Si/ZnO-120 °C, and (g) EDS images of the P–Si/ZnO heterojunction.

relationship between $\ln(C_0/C)$ and the illumination time as well as the pseudo-first-order reaction rate constant (k), which enables quantification of the photocatalytic performance of the sample.[31–33] The degradation rate constant of P–Si/ZnO-90 °C under UV and visible light irradiation is 7.19 min^{-1}, which is 12.2 times, 7.8 times, 6.7 times, 6.1 times, and 5.5 times higher than those of P–Si, P–Si/ZnO-70 °C, P–Si/ZnO-80 °C, P–Si/ZnO-100 °C, and P–Si/ZnO-120 °C, respectively. Meanwhile, to verify the degradation performance of the P–Si/ZnO-90 °C heterojunction to different organic pollutants, the P–Si/ZnO-90 °C heterojunction was used to degrade methyl orange and tetracycline hydrochloride with a concentration of 5 mg L^{-1} using the P–Si/ZnO-90 °C heterojunction for 2 hours, and the degradation rates were 39% and 72%, respectively (see Fig. S1†).

Apart from the catalyst activity, the repeatability and stability of the material are also crucial in practical applications. As shown in Fig. 6, the recyclability and stability of P–Si/ZnO-90 °C were evaluated under the same experimental conditions. It is noteworthy that the material we use is a block sample, and simple rinsing is sufficient for recovery, without the need for additional complex separation steps, such as centrifugation. After 20 cycles of use, the photocatalytic degradation rate of P–Si/ZnO-90 °C can still remain above 70%, demonstrating superior stability and reusability.

3.3 Photoelectric chemical analysis

To further explore the reasons for the enhanced efficiency of photocatalytic degradation of RhB by the P–Si/ZnO heterojunction, electrochemical tests were performed on the samples. Fig. 7a shows the linear sweep voltammetry (LSV) curves of P–Si/ZnO-90 °C, which has the most optimal photoelectric current characteristics at a bias voltage of 1.5 V, with a photoelectric current density of 356 μA cm^{-2}, while the photoelectric
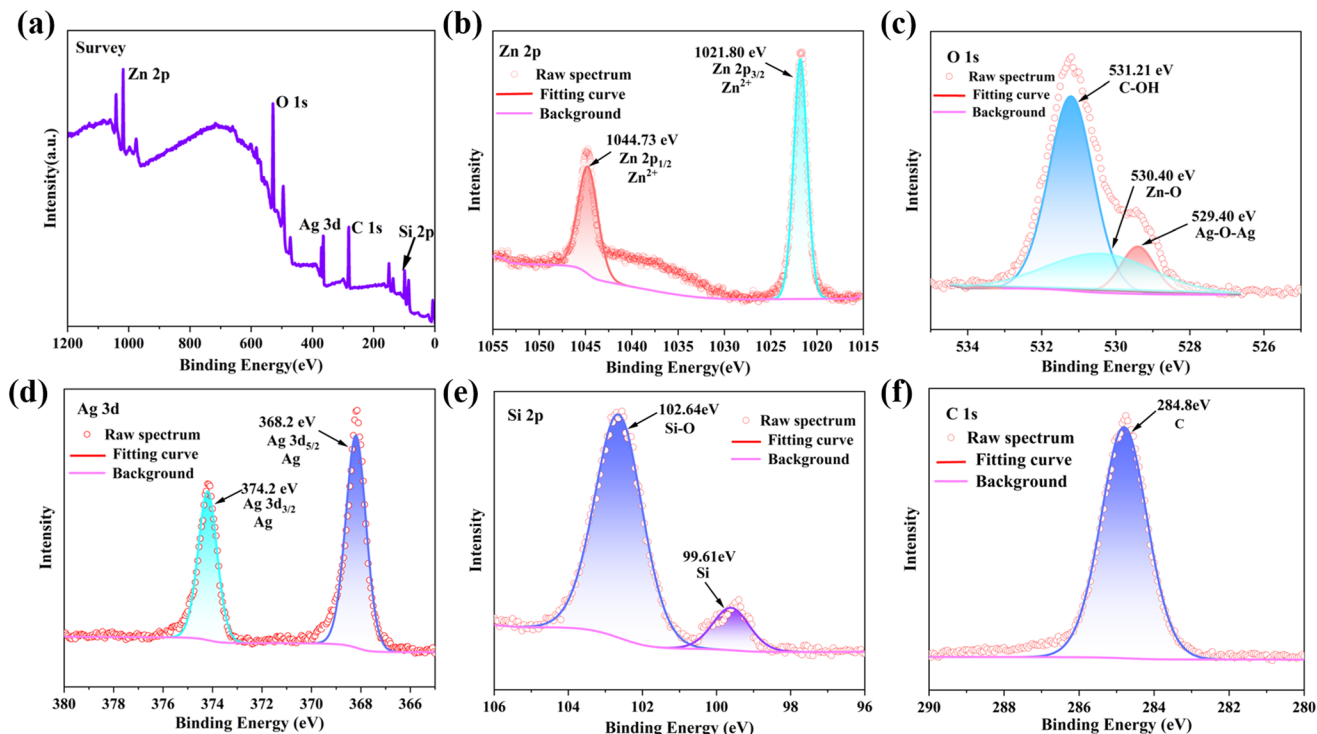
Fig. 4 XPS spectra of the P−Si/ZnO heterojunction: (a) survey, (b) Zn 2p, (c) O 1s, (d) Ag 3d, (e) Si 2p, and (f) C 1s.
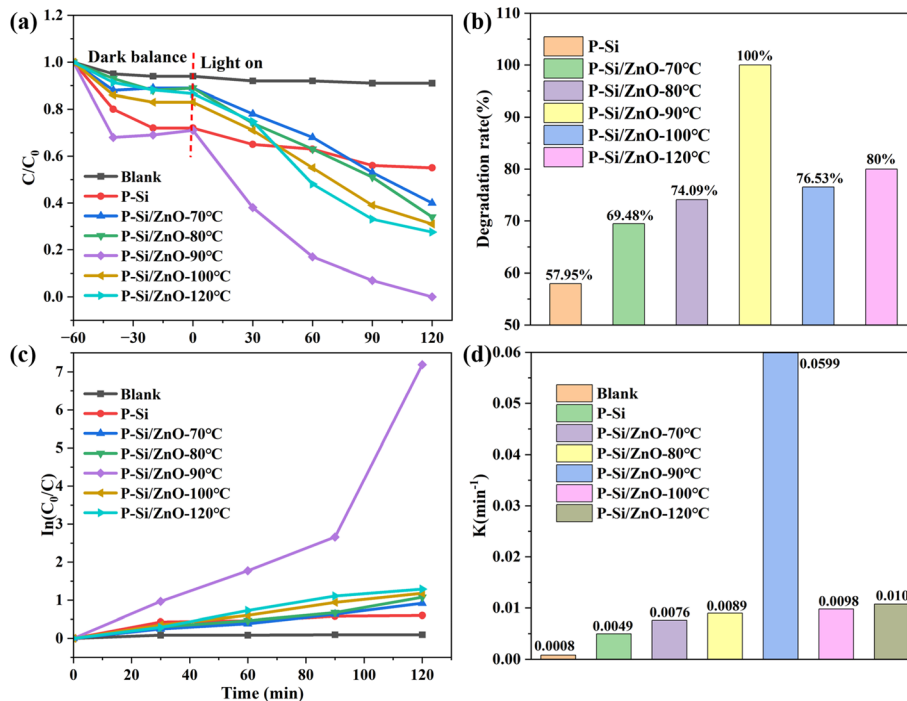

Fig. 5 Curves of photocatalytic degradation of RhB with different catalysts (a and b) and the apparent reaction rate constants (*k*) (c and d). Experimental conditions: RhB, 5 mg L^{-1}.

current density of P−Si is the lowest, at only 50 μA cm^{-2}. This indicates that the introduction of ZnO can enhance the photoelectric performance of P−Si, and the complete 1D ZnO hexagonal prism structure is more conducive to the directional

transmission of carriers, thereby improving the migration rate of electrons in the electrode and electrolyte, which has a relatively high photocurrent density. The radius of the circular arcs in the Nyquist plot can reflect the electron transfer
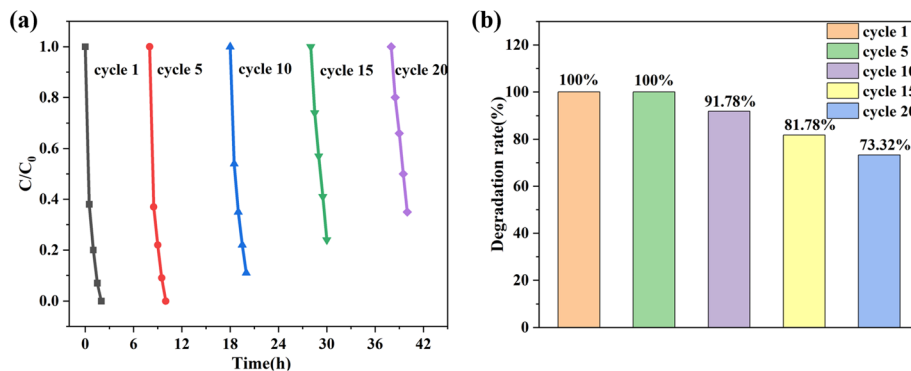
Fig. 6 Reusability of the P–Si/ZnO heterojunction for photocatalytic degradation of RhB (a and b).
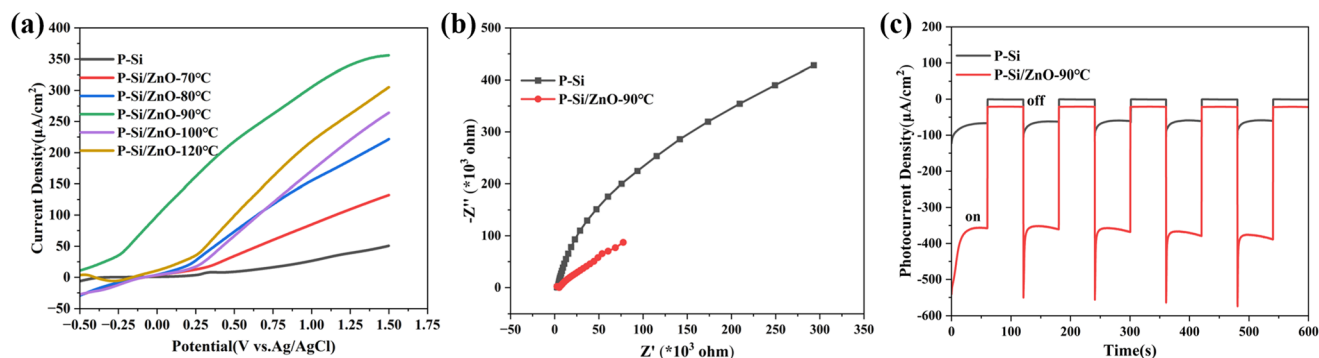

Fig. 7 (a) Linear sweep voltammetry (LSV) curves, (b) Nyquist impedance plots and transient photocurrent responses (c) of P–Si and P–Si/ZnO heterojunction.

efficiency within the electrode.[34,35] The smaller the radius of the arc, the faster the generation rate of photogenerated charge carriers within the sample, the lower the impedance inside the sample, and the higher the electron transfer efficiency within the electrode. According to Fig. 7b, the P–Si/ZnO has a smaller arc radius, indicating lower electron movement impedance. This results in higher efficiency for electron–hole pair separation and electron transport, thereby displaying superior photoelectrochemical properties. Finally, the i–t curves of P–Si and P–Si/ZnO are shown in Fig. 7c, and under illumination conditions, the photocurrent response of P–Si/ZnO is increased relative to the single material. This indicates that the composite of P–Si and ZnO has more efficient light-induced electron–hole pair separation efficiency and faster interfacial charge transfer, thereby improving the catalytic performance of the catalyst. In summary, the reason for the improved photocatalytic degradation efficiency after constructing the P–Si/ZnO heterojunction can be attributed to the enhanced light response capability and the improved separation and migration efficiency of electron–hole pairs.

3.4 Mechanism of photocatalytic degradation

In order to study the photocatalytic degradation mechanism of P–Si/ZnO, the following formula was used to investigate the energy band structure of the material.[36,37] Based on the above formula and Fig. 8a and b, the E_g values of P–Si and ZnO were 1.21 eV and 3.2 eV, respectively, and the X values of P–Si and ZnO were 4.77 V and 5.79 V, respectively. As a result, the E_{VB} and E_{CB} of P–Si and ZnO can be obtained as (0.88, −0.34) and (2.89, −0.31), respectively (Fig. 9a). Their valence band edge potentials are all greater than 0.6 V ($vs.$ NHE), indicating that both P–Si and ZnO can photocatalytically degrade RhB thermodynamically. At the same time, the quenching experiment was carried out to explore the main active species in the reaction during the degradation of RhB by P–Si/ZnO. In the quenching experiments, AgNO$_3$, isopropyl alcohol (IPA), p-benzoquinone (BQ), and ethylenediaminetetraacetic acid disodium salt (EDTA-2Na) were used as effective quenchers for e$^-$, ·OH, ·O$_2^-$, and h$^+$, respectively.[38–40] The experimental results are shown in Fig. 8a. After the addition of IPA, BQ, and EDTA-2Na, the photocatalytic degradation process of RhB is significantly inhibited, indicating that ·OH, ·O$_2^-$, and h$^+$ are the primary active species involved in the reaction.

$$\alpha h\nu = A(h\nu - E_g)^{n/2} \tag{1}$$

$$E_{VB} = X - E^e + 0.5E_g \tag{2}$$

$$E_{CB} = E_{VB} - E_g \tag{3}$$

Based on the above analysis, we propose the degradation mechanism for RhB photocatalytic degradation by P–Si/ZnO,
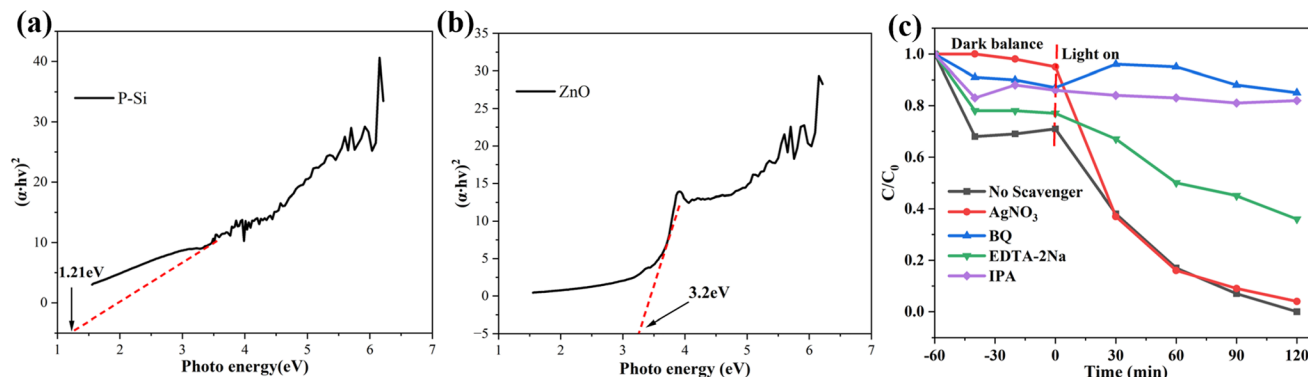
Fig. 8 (a) and (b) Energy band diagrams of P–Si and P–Si/ZnO, and (c) effect of different scavengers on the photodegradation of RhB by the P–Si/ZnO heterojunction.
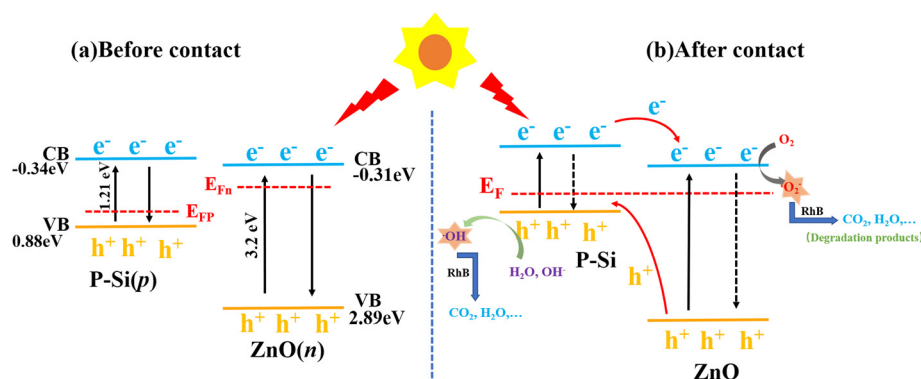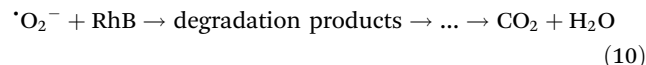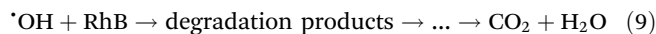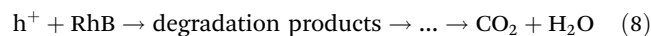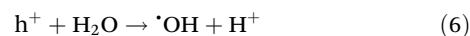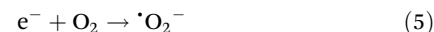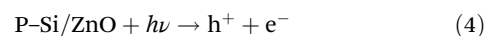

Fig. 9 Mechanism of photocatalytic degradation of RhB by the P–Si/ZnO heterojunction.

which is described in Fig. 9. Before contact between p-type P–Si and n-type ZnO, the Fermi level of ZnO is higher than that of P–Si, which is not conducive to the separation and migration of carriers. After contact between P–Si and ZnO, a p–n heterojunction is formed. Due to the concentration gradient of photogenerated carriers, the photo-generated electrons flow from the conduction band of p-type P–Si to the conduction band of n-type ZnO, while holes flow from the n-region to the p-region. As a result, the Fermi level of ZnO (E_{Fn}) continuously moves down, and the Fermi level of P–Si (E_{Fp}) continuously moves up until $E_{Fn} = E_{Fp}$.[41,42] During this process, the energy bands of P–Si and ZnO bend, and a built-in electric field is formed at the junction.[16,35] Under the combined action of electric field and photons, the negatively charged photo-generated electrons and positively charged holes are separated and migrate to different positions on the catalyst surface to participate in redox reactions. Specifically, the photo-generated holes with strong oxidation ability can directly oxidize RhB, while dissolved oxygen adsorbed on the catalyst surface can capture electrons to form superoxide radicals ($^{\bullet}O_2^{-}$), and holes can oxidize OH^{-} and H_2O adsorbed on the catalyst surface to form hydroxyl radicals ($^{\bullet}OH$). The formed $^{\bullet}O_2^{-}$ and $^{\bullet}OH$ can then degrade RhB into less toxic products, and ultimately to CO_2

and H_2O.[43-46] The following chemical equations represent the principal steps of the reasonable photocatalytic reaction.

$$P–Si/ZnO + h\nu \rightarrow h^{+} + e^{-} \tag{4}$$

$$e^{-} + O_2 \rightarrow {}^{\bullet}O_2^{-} \tag{5}$$

$$h^{+} + H_2O \rightarrow {}^{\bullet}OH + H^{+} \tag{6}$$

$$h^{+} + OH^{-} \rightarrow {}^{\bullet}OH \tag{7}$$

$$h^{+} + RhB \rightarrow \text{degradation products} \rightarrow ... \rightarrow CO_2 + H_2O \tag{8}$$

$${}^{\bullet}OH + RhB \rightarrow \text{degradation products} \rightarrow ... \rightarrow CO_2 + H_2O \tag{9}$$

$${}^{\bullet}O_2^{-} + RhB \rightarrow \text{degradation products} \rightarrow ... \rightarrow CO_2 + H_2O \tag{10}$$

4. Conclusion

In summary, the P–Si/ZnO heterojunction synthesized by carbon catalytic etching and electroless chemical deposition based on the galvanic cell-driven mechanism exhibits excellent photoresponse performance and enhances the active sites for photocatalytic reactions. Experimental results indicate that

compared to the single P–Si material, the P–Si/ZnO heterojunction significantly enhances the degradation ability of RhB under ultraviolet and visible light irradiation. At a deposition temperature of 90 °C and using 5 mg L^{-1} RhB as a simulated pollutant, P–Si/ZnO-90 °C achieved a degradation rate of 100% for RhB within 2 hours. Additionally, after 20 cycles of use, the photocatalytic degradation rate is still maintained above 70%, showing superior stability and reusability. Hence, this study paves a new path for the development and utilization of semiconductor materials in the environmental field and offers a wide range of applications.

Conflicts of interest

The authors declare no conflict of interest.

Acknowledgements

References

1 Y. Sun, P. Tian, D. Ding, Z. Yang, W. Wang and H. Xin, *Appl. Catal., B*, 2019, **258**, 117985.

2 Z. Wang, K. Wang, Y. Li, L. Jiang and G. Zhang, *Appl. Surf. Sci.*, 2019, **498**, 143850.

3 L. Feng, X. Li, L. Gan and J. Xu, *Electrochim. Acta*, 2018, **290**, 165–175.

4 A. Mizrahi and I. M. Litaor, *Desalin. Water Treat.*, 2014, **52**, 5264–5275.

5 Y. Feng, Z. Zhang, Y. Zhao, L. Song, X. Wang and S. Yang, *Bioresour. Technol.*, 2019, **283**, 1–9.

6 R. T. Lawrence, M. P. Croxall, C. Lu and M. C. Goh, *Nanoscale*, 2023, **15**, 2788–2797.

7 K. Wang and T. He, *Nanoscale*, 2023, **15**, 12398–12405.

8 Z. H. Jabbar and S. Esmail Ebrahim, *Environ. Nanotechnol., Monit. Manage.*, 2022, **17**, 100666.

9 J. Qiu, M. Li, M. Ding and J. Yao, *Renewable Sustainable Energy Rev.*, 2022, **154**, 111820.

10 H. Wang, X. Li, X. Zhao, C. Li, X. Song and P. Zhang, *Chin. J. Catal.*, 2022, **43**, 178–214.

11 P. Zhang, J. Wang, J. Hu, Z. Tong, Y. Wang and S. Liu, *Nanoscale*, 2023, **15**, 10693–10704.

12 Y. Wang, S. Liang, C. Zuo, H. Fang, G. Dong and X. Sheng, *Nanoscale*, 2023, **15**, 5230–5240.

13 Y. Li, J. Wang, Y. Yang, Y. Zhang, D. I. He and Q. An, *J. Hazard. Mater.*, 2015, **292**, 79–89.

14 M. A. Hamza, S. A. Abd El-Rahman and Z. M. Abou-Gamra, *Opt. Mater.*, 2022, **124**, 111987.

15 G. Wang, Z. Li, M. Li, Y. Feng, W. Li and S. Lv, *Ceram. Int.*, 2018, **44**, 1291–1295.

16 N. T. Hoa, V. van Cuong and N. D. Lam, *Mater. Chem. Phys.*, 2018, **204**, 397–402.

17 X. Lin, *Synthesis and Performance Study of Silicon Nanowire-Based Core-Shell Structure Composite Photocatalyst*, Fuzhou University, Fuzhou, Fujian, 2018.

18 W. J. Chen, K. C. Hsu, T. H. Fang, T. H. Chen and M. H. Li, *Curr. Appl. Phys.*, 2022, **38**, 1–6.

19 K. C. Hsu, T. H. Fang, Y. J. Hsiao and Z. J. Li, *J. Alloys Compd.*, 2021, **852**, 157014.

20 M. Le Pivert, N. Martin and Y. Leprince Wang, *Crystallography*, 2022, **12**, 308.

21 J. Singh, S. Kumar, A. K. Rishikesh, A. K. Manna and R. K. Soni, *Opt. Mater.*, 2020, **107**, 110138.

22 N. Rangelova, L. Aleksandrov and S. Yaneva, *Mater. Today: Proc.*, 2022, **61**, 1272–1279.

23 J. Wen, N. Li, P. Lin, Y. Han, G. Chen and L. Bai, *Phys. E*, 2021, **134**, 114913.

24 J. Lan, B. He, C. Haw, M. Gao, I. Khan and R. Zheng, *Appl. Surf. Sci.*, 2020, **529**, 147023.

25 A. P. P. Da Rosa, R. P. Cavalcante, T. F. Da Silva, F. Gozzi, C. Byrne and E. McGlynn, *J. Nanosci. Nanotechnol.*, 2020, **20**, 1177–1188.

26 Y. Zeng, X. Chen, Z. Yi, Y. Yi and X. Xu, *Appl. Surf. Sci.*, 2018, **441**, 40–48.

27 L. S. Wang, Y. L. Wei, C. L. Chen and S. Yang, *Dalton Trans.*, 2021, **50**, 3011–3019.

28 C. Chevalier-César, M. Capochichi-Gnambodoe and Y. Leprince-Wang, *Appl. Phys. A*, 2014, **115**, 953–960.

29 J. Yang, J. Wang, X. Li, D. Wang and H. Song, *Catal. Sci. Technol.*, 2016, **6**, 4525–4534.

30 H. van Dang, Y. H. Wang and J. C. Wu, *Appl. Catal., B*, 2021, **296**, 120339.

31 T. Phongamwong, N. Barrabés, W. Donphai, T. Witoon, G. Rupprechter and M. Chareonpanich, *Appl. Catal., B*, 2023, **325**, 122336.

32 I. Ahmad, M. Aslam, U. Jabeen, M. N. Zafar, M. N. K. Malghani and N. Alwadai, *Inorg. Chim. Acta*, 2022, **543**, 121167.

33 M. G. Kim, J. E. Lee, K. S. Kim, J. M. Kang, J. H. Lee and K. H. Kim, *New J. Chem.*, 2021, **45**, 3485–3497.

34 L. D. Bastatas, P. Wagle, E. Echeverria, J. D. Slinker and D. N. McIlroy, *Nanotechnology*, 2019, **30**, 234006.

35 R. Pietruszka, G. Luka, K. Kopalko, E. Zielony, P. Bieganski and E. Placzek-Popko, *Mater. Sci. Semicond. Process.*, 2014, **25**, 190–196.

36 S. Anjelin Ursula Portia, S. Rajkumar, E. Elanthamilan, J. Princy Merlin and K. Ramamoorthy, *Inorg. Chem. Commun.*, 2020, **119**, 108051.

37 Y. Huang, L. Nengzi, X. Li, L. Meng, Q. Song and X. Cheng, *Mater. Sci. Semicond. Process.*, 2020, **109**, 104932.

38 D. Zhang, J. Li, Q. Wang and Q. Wu, *J. Mater. Chem. A*, 2013, **1**, 8622.

39 Y. Hong, A. Ren, Y. Jiang, J. He, L. Xiao and W. Shi, *Ceram. Int.*, 2015, **41**, 1477–1486.

40 L. Hu, G. Deng, W. Lu, S. Pang and X. Hu, *Appl. Surf. Sci.*, 2017, **410**, 401–413.

41 Y. Yang, L. Sun, W. Zhan, X. Wang and X. Han, *J. Mater. Chem. A*, 2021, **9**, 4310–4316.

42 H. Song, R. Wu, J. Yang, J. Dong and G. Ji, *J. Colloid Interface Sci.*, 2018, **512**, 325–334.

43 N. Chandel, K. Sharma, A. Sudhaik, P. Raizada, A. Hosseini-Bandegharaei and V. K. Thakur, *Arab. J. Chem.*, 2020, **13**, 4324–4340.

44 Y. Li, Y. Li, Y. Yin, D. Xia, H. Ding and C. Ding, *Appl. Catal., B*, 2018, **226**, 324–336.

45 L. T. Nguyen, D. V. N. Vo, L. T. Nguyen, A. T. Duong, H. Q. Nguyen and N. M. Chu, *Environ. Technol. Innovation*, 2022, **25**, 102130.

46 Q. You, C. Zhang, M. Cao, B. Wang, J. Huang and Y. Wang, *Appl. Catal., B*, 2023, **321**, 121941.